Materials Advances

PAPER

Check for updates

Unveiling superior creatinine detection: advanced electrochemical biosensor with remarkable sensitivity

Taotao Liang, [ID]†*[a] Yan Zhang,†[a] Junfeng Guo,†[a] Jingtong Lv,[a] Tao Hu, [ID][c] Xiaogang Guo, [ID]*[b] Chuyue Tang*[a] and Lin Guo*[a]

The prompt and precise detection of creatinine is essential, as it serves as a critical biomarker for evaluating the severity of kidney disease. This study introduces the development of an innovative non-enzymatic electrochemical biosensor designed for the sensitive detection of creatinine. The biosensor was created by functionalizing carbon nanotubes with anhydrous copper acetate through a simple one-step hydrothermal method. The unique properties of carbon nanotubes provide numerous adsorption sites that promote specific coordination interactions between copper nanoparticles and creatinine, thereby establishing the foundation for the sensor's enhanced sensitivity. The sensor exhibits remarkable specificity, with the creatinine concentration demonstrating a linear response within the range of 0.01 mM to 1 mM, and an exceptional sensitivity of 8617.86 $\mu A\ mM^{-1}\ cm^{-2}$. Notably, superior sensors of this type have been documented, particularly within the narrower concentration range of 0.01 mM to 0.05 mM, indicating that this sensor outperforms others in its class. Furthermore, density functional theory (DFT) calculations, encompassing electron state density, differential charge density, and adsorption energy assessments, corroborate the material's outstanding properties and elucidate the underlying detection mechanism. Furthermore, a range of flexible creatinine sensors was developed utilizing 3D printing and sputtering techniques. These sensors demonstrated exceptional sensing performance, thereby expanding the potential applications of the material and effectively highlighting its intrinsic properties.

Introduction

The kidneys are essential organs in the human body, performing functions such as removing metabolic wastes, reabsorbing certain nutrients, and regulating blood pressure and erythropoiesis.[1] Creatinine (Cr), as a prognostic marker, is generated in muscle tissue by the irreversible non-enzymatic dehydration reaction of creatine and released into the bloodstream to be excreted in urine.[2] Creatinine levels in human serum typically range from 44 to 133 μM, and any creatinine levels beyond this range usually indicate renal, muscular, or thyroid-related diseases. Creatinine values above 500 μM are associated with severe kidney damage, and below 40 μM indicate an abnormal reduction in muscle mass.[3] Therefore, it can assess renal function, chronic kidney disease, and muscle disease. Recent clinical studies have further

emphasized the significance of creatinine as a prognostic marker, with elevated levels showing strong correlation with cardiovascular complications in patients with chronic kidney disease (CKD).[4–6] Current detection methods for creatinine include spectrophotometry, high-performance liquid chromatography, spectral analysis, chemiluminescence immunoassay, electrochemical sensing, and other approaches.[7] Among them, electrochemical biosensing technology, as a new technology for biomolecule detection, combines the advantages of the previous methods, including high sensitivity, low detection limit, high selectivity, simple operation, and other benefits, so the use of electrochemical sensing technology for the detection of various types of biomolecules has aroused great interest.[8–10] Some studies highlighted that electrochemical sensors have witnessed a 35% increase in clinical adoption over the past five years due to their real-time monitoring capabilities.[11–13] Recently, various methods have been created for identifying creatinine through enzymatic and non-enzymatic electrochemical sensing techniques.[3,14,15] Dasgupta *et al.*, by utilizing creatinine deiminase, broke down creatinine into 1-methyl glycol acetone urea, allowing creatinine molecules to be detected *via* an electric current signal produced when it was paired with cobalt ions.[16] However, enzyme

a Third Military Medical University Southwest Hospital, Orthopedic Surgery and Clinical Laboratory Medicine, Chongqing Sports Medicine Center, Chongqing, China. E-mail: liangtaotao2018@foxmail.com
b Yangtze Normal University, Chongqing, China
c Suzhou University of Science and Technology, Institute of Materials Science and Devices, Suzhou, Jiangsu, China
† Taotao Liang, Yan Zhang and Junfeng Guo contributed equally to this work.

electrochemical sensors suffer from high costs and poor long-term storage stability, so non-enzymatic sensors based on nanomaterials have emerged, such as the use of nanomaterials such as ZIF-8/PEDOT: PSS/ITO and CNT/FA/Ag NPs for creatinine detection.[17,18] The development of 3D printing technology also offers promising innovations for fabricating biosensors and their components. Biosensor structures can be customized using this technology, offering the advantages of low cost, rapid prototyping and manufacturing, and minimal waste.[19,20] 4D-printed sensors that self-assemble upon hydration, AI-optimized designs achieving 300% sensitivity enhancement, and sustainable materials like chitosan-based bioinks which degrade in 30 days, are some examples.[21–23] The technology's design freedom and multi-material capability position bio-printing as the cornerstone of next-generation biosensor development.

Along with the development of nanotechnology, the emergence of various nanomaterials such as carbon nanomaterials, metal nanoparticles, and metal oxides has contributed significantly to the development of electrochemical biosensors. Among them, carbon nanotubes (CNTs) are a kind of carbon nanomaterial with excellent properties such as large aspect ratios, high surface areas, and electrical conductivity, which have remarkable electron transfer ability in electrochemical reactions, and combining them with nanomaterials with different properties can effectively enhance the electrochemical performance.[24,25]

Metal oxide nanostructures have the advantages of both metals and nanomaterials, including large active specific surface areas and very high electron transfer efficiency. Among them, the electrochemical properties of copper oxide are susceptible to the external environment, and its application to biosensors can significantly improve the response speed and sensitivity of biosensors.[26] Recent advances in creatinine sensing employ novel materials and detection strategies to transform kidney disease diagnostics.[27–30] Flexible 3D conductive polymers (PPy/V_2O_5/TiO_2) enable enzyme-less electrochemical detection, while molecularly imprinted MXene/AuNPs offer ultra-specific recognition. Solid-state nanopores with enzymatic pH modulation achieve miniaturized sensing, and Prof. Li's rGO/PDA-MIP platform breaks sensitivity barriers for simultaneous creatinine/urea monitoring. The integration of nanocomposites, imprinting strategies, and nanofluidic systems enables portable, cost-effective devices suitable for point-of-care use, particularly in resource-limited settings. Together, they represent a paradigm shift toward accessible, high-performance kidney disease monitoring through multi-analyte detection, user-friendly operation, and robust performance in complex biological matrices.

In this study, we have utilized a simple one-step hydrothermal synthesis method for functionalized CNTs and copper nanoparticles to modify electrodes to develop non-enzymatic electrochemical biosensors for the highly sensitive detection of creatinine. This biosensing mechanism combines copper ions and creatinine to form a creatinine-copper coordination compound, which leads to a linear relationship between creatinine levels and the peak oxidation current. CNT offers numerous adsorption sites on their surface for copper ions, significantly

enhancing the sensor's performance. The proposed creatinine biosensor has an extremely high sensitivity toward creatinine of 8617.86 μA mM^{-1} cm^{-2}. The DFT calculations, including electron state density, differential charge density, and adsorption energy calculation, verified the material's excellent properties and inferred the material's detection mechanism and creatinine. In addition, various flexible creatinine sensors were fabricated using 3D printing and sputtering techniques. These sensors exhibited excellent sensing performance, broadening the material's potential applications and fully showcasing its inherent properties.

Experimental section

Materials and reagents

Creatinine, glucose, uric acid, urea, NaCl, KCl, anhydrous copper acetate, sodium hydroxide, and phosphoric acid, potassium ferrocyanide(II) were purchased from Sigma-Aldrich.

The ELISA kit for creatinine was purchased from Fisher Scientific. Iron(III) chloride, potassium ferricyanide(III), silver nitrate and 0.1 M phosphate-buffered saline (PBS) (pH 7.4) were purchased from Aladdin Co, Polyethylene terephthalate (PET) films, carbon ink (5 wt%) and silver ink (25 wt%) were purchased from the Taobao website. All chemicals were used as received. An anhydrous copper acetate solution was configured as a 1 mg mL^{-1} solution, sodium hydroxide and phosphoric acid solutions were configured as buffers of pH 4 to pH 9, and diluted 5% sodium solutions were reduced to 0.5%. The remaining reagents used in the study, including deionized water (DI) from the Milli-Q water purification system, were used as received.

Preparation of the CNT/CuO@Cu_2O nanocluster ink

CNT/CuO@Cu_2O were synthesized using the hydrothermal synthesis method. First, 0.01 g of CNT and 0.075 g $Cu(CH_3COOH)_2$ were dissolved in 9 mL of deionized water. Then, 15 mL of ethylene glycol and 6 mL of ethanol were gradually added into the solution under continuous stirring ultrasonication for 10 minutes to mix well for 2 h at room temperature. The resulting mixture was then subjected to an oven treatment at 120 °C for 8 hours, after which it was allowed to cool overnight. Once the reaction was completed, the blank supernatant was discarded, and 20 ml of deionized water was added to the sediment. This was followed by vigorous shaking using a vortex machine for 2 min. The impurities mixture was washed multiple times with deionized water by centrifugation at 2000 relative centrifugal force (RCF) for 5 min for each cycle until solvent-free stratification.

To prepared CNT/CuO@Cu_2O nanocluster ink, an aliquot of the prepared suspension was dried and diluted to a concentration of 1 mg ml^{-1} for further use (Fig. S1).

Construction and modification of the CNT/CuO@Cu_2O/GCE sensing platform

The biorecognition interface and working electrode were assembled face-to-face on the glassy carbon electrode (GCE). We first polished the GCE using a polishing chamois and 0.3 μM and

0.05 μM aluminum powders to create a mirror-like surface. Then, a 1 mg mL^{-1} suspension of CNT/CuO@Cu$_2$O was prepared by sonication until it was evenly distributed. To form the sensing platform interface, 10 μL drops of this suspension were added to the treated GCE and dried at room temperature. Then, 5 μL of a 0.5% Nafion solution was added dropwise. This process resulted in the formation of a CNT/CuO@Cu$_2$O/GCE electrode, which was utilized as the working electrode. Furthermore, CNT/GCE and Cu(CH$_3$COOH)$_2$/GCE were prepared using the same method, which acts as a competitive sensing electrode.

Physical and electrochemical characterization of the biosensor

The surface morphology of the materials was characterized by FE-SEM, which provided detailed images of the samples' surfaces. The crystal structure of the materials was analyzed using XRD, which revealed the unique patterns and structures of the different phases present in the materials. FT-IR and XPS were used to analyze compositions and determine elemental valences and relative contents.

This study utilized a silver/silver chloride (Ag/AgCl) electrode as the reference electrode, while a platinum (Pt) wire electrode served as the counter electrode. Phosphate buffer (0.01 M PBS, pH = 7.4) was used as an electrolyte, and the electrochemical measurements were conducted under air-saturated and nitrogen-saturated conditions. The modified working electrode was immersed in 10 mL of PBS solution, and a creatinine solution with a concentration gradient ranging from 0.01 mM to 1 mM was added sequentially. The working electrodes were subsequently utilized for creatinine detection. The working electrode of its 3D electrode was coated with 100 μL of PBS electrolyte. A solution of creatinine with a concentration gradient ranging from 0.01 mM to 30 mM was added sequentially to the working electrode. The electrodes used in these studies were prepared on the same day with oven drying, and stored at 4 °C.

To characterize the electrode performances of GCE, CNT/GCE, Cu(CH$_3$COOH)$_2$/GCE, and CNT/CuO@Cu$_2$O/GCE, and to confirm the surface modification after 3D printing of bio-3D printing CNT/CuO@Cu$_2$O flexible sensors, differential pulse voltammetry (DPV) and OCP-EIS reading were executed in 0.2× PBS(pH7.4) containing 2.0 mM K$_4$Fe(CN)$_6$/K$_3$Fe(CN)$_6$ (1:1) under the following conditions: potential range, −0.4 to 0.4 V; pulse width, 0.2 s; incremental potential, 4 mV; amplitude, 50 mV; frequency range, 0.1–10^6 Hz; amplitude, 5 mV.

In addition, the electrode surfaces of GCE, CNT/GCE, Cu(CH$_3$COOH)$_2$/GCE, and CNT/CuO@Cu$_2$O/GCE were compared through cyclic voltammetry(CV) characterization in the range of −0.6 to 0.6 V at different scan rates (10, 20, 30, 50, 70, 100, 200 and 300 mV s^{-1}) in artificial urine (0.2 × PBS, pH 7.4). All electrochemical measurements of the working electrode were performed at room temperature in artificial sweat unless otherwise noted.

DFT calculations

Our computational investigations, conducted within the framework of spin-polarized density functional theory (DFT), were implemented using the Vienna *ab initio* simulation package (VASP). This computational methodology utilizes a plane-wave basis set in conjunction with the projector augmented-wave (PAW) technique. The electronic exchange and correlation effects were treated employing the generalized gradient approximation (GGA) with the Perdew–Burke–Ernzerhof (PBE) functional. Additionally, van der Waals interactions were included by integrating Grimme's DFT-D3 correction scheme into the calculations. To prevent artificial interactions between periodic replicas, an 18 Å vacuum buffer was carefully incorporated into the simulation setup. The energy cutoff was set at 450 eV to ensure a balance between computational precision and efficiency. Brillouin-zone integration was meticulously carried out using a Γ-centered Monkhorst–Pack k-point mesh with a 2 × 2 × 1 configuration, enabling a thorough sampling of reciprocal space. Structural optimization was pursued until the forces on each atom reached a threshold below 0.02 eV Å^{-1} to ensure structural stability. Moreover, the energy calculations were converged to a stringent criterion of 10^{-5} eV to guarantee the accuracy of our computational outcomes.

Applied flexible design

Firstly, SOLIDWORKS and CAD modeling software were used to create a flexible sensor model with dimensions of 12 × 30 mm^2, 1 mm, and 50 nm thicknesses and working electrode areas of 0.25 mm^2 and 0.0625 mm^2, respectively. Carbon paste and a CNT/CuO@Cu$_2$O suspension were mixed appropriately to create the composite inks. The composite inks and silver paste were loaded into two cryogenic extruders for subsequent printing, in which the composite inks were utilized for the working electrodes and counter electrodes. The silver paste served as the reference electrode. The composite ink and silver paste were loaded into two low-temperature extruders for printing. The composite ink served as the working electrode and counter electrode, while the silver paste was the reference electrode. Polyethylene terephthalate (PET) was cut into 10 × 10 cm^2 squares and placed on the printing platform as the flexible sensor substrate. The corresponding patterns were printed based on the designed 3D models using a bio-3D printing system, cut to the specified dimensions, and dried in an oven at 60 °C for spare parts. The flexible gold electrode was created by placing a stainless steel mask plate, 0.5 mm thick, on a 10 × 10 cm^2 PET substrate and sputtering a 50 nm gold layer using sputtering apparatus. A layer of silver paste was then applied to the reference area as a reference electrode, which was cleaned with deionized water before use. The modification of the working electrode was as described above.

Creatinine detection in a kidney injury animal model

Male Sprague–Dawley rats were purchased from the experimental animal center of Third Military Medical University (Chongqing, China). The age of rats ranged from 4–6 weeks (body weight 200–250 g). All rats were housed in a specific pathogen-free environment in the animal facility of Southwest Hospital (Chongqing, China) in accordance with the Guide for the Care and Use of Laboratory Animals. An animal model of cisplatin-induced acute kidney injury (AKI) was established in rats by intraperitoneal injection of cisplatin (10 mg kg^{-1}, single injection; Sigma-Aldrich).

Rats were anesthetized for euthanasia and blood was harvested 3 days after cisplatin injection. Specifically, the animals were fixed in a supine position, the index finger detected the highest part of the heartbeat, and the hair on the skin surface was cut off, and disinfected with 75% alcohol. Use a 9# needle to pierce the heart at 45 degrees, then move the needle up and down gently. After the blood enters the barrel, fix the position of the syringe to take blood. All animal studies were approved by the Ethics Committee of Army Medical University, PLA (Chongqing, China). Whole blood samples from acute kidney injury model rats were collected in 15 mL centrifuge tubes and stood at 4 °C for 12 hours. Then, the blood samples were separated by centrifugation at 3000 rpm for 90 min. The upper serum was collected, and the samples were equally divided into two parts for colorimetric detection and electrochemical detection, respectively, and instantly stored at −80 °C for serum creatinine testing.

AKI rat serum samples for ELISAs

The evaluation of the CNT/CuO@Cu$_2$O flexible sensor for serum creatinine monitoring in serum samples for rat AKI models followed all the ethical regulations according to the Animal Ethical Statement (AMUWE C20211973), and the experimental animal production license number of our unit is SCXK(Chongqing)20170002, and the use license number is SYXK(Chongqing)20170002. Colorimetric detection was carried out using a Creatinine Assay Kit (Sigma-Aldrich, Missouri, USA). Briefly, serum samples were first deproteinized with a 10 kDa MWCO spin filter, serum and appropriate reaction mixture were mixed into a 96-well plate, then mixed well using a horizontal shaker, and the reaction was incubated at 37 °C for 60 minutes, and finally the absorbance was measured at 570 nm (A570).

Results and discussion

Characterization of CNT/CuO@Cu$_2$O nanoclusters

After CNT/CuO@Cu$_2$O nanocomposites were prepared using a hydrothermal method, their morphology, structure, and valence changes were analyzed through field emission scanning electron microscopy (FE-SEM), X-Ray diffraction (XRD), and Fourier transform infrared spectroscopy (FT-IR) techniques (Fig. 1). FESEM first characterized the prepared samples for microscopic morphology. It can be seen that the untreated Cu(CH$_3$COOH)$_2$ and CNT showed a stacked lamellar structure and intertwined dense mesh structure, respectively (Fig. 1B and C). Many copper oxide spherical nanoparticles were observed as clusters attached to the CNT of the dense mesh structure after the hydrothermal reaction (Fig. 1D). The material's specific surface area and pore size distribution were analyzed using nitrogen adsorption–desorption experiments. An energy dispersive X-ray spectrometer (EDS) analyzed the samples to obtain a carbon atom mass of 55.16%, an oxygen atom mass of 12.9%, and a copper atom mass of 31.94% (Fig. S1). CNT and CNT/CuO@Cu$_2$O exhibit H3 hysteresis loops in the relative pressure range of 0.5–0.8, indicating that the pore structure primarily
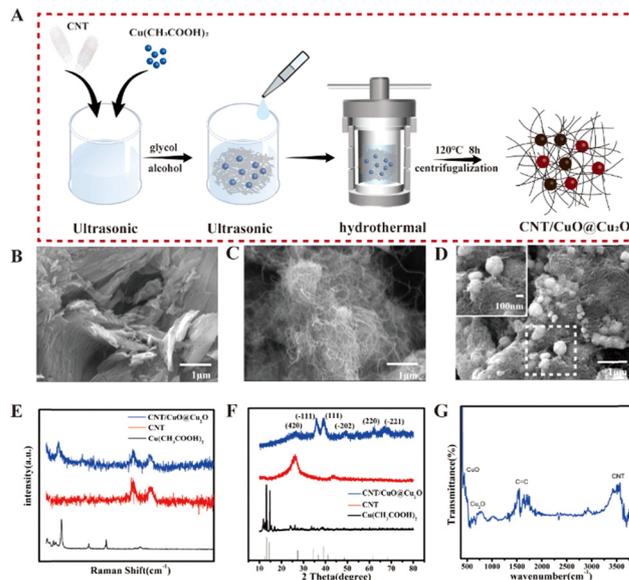

Fig. 1 (A) Fabrication process of CNT/CuO@Cu$_2$O materials; FE-SEM image of (B) Cu(CH$_3$COOH)$_2$; (C) CNT; (D) CNT/CuO@Cu$_2$O composites; (E) the Raman spectra; (F) XRD spectra of CNT, Cu(CH$_3$COOH)$_2$ and CNT/CuO@Cu$_2$O composites; (G) FT-IR spectra of CNT/CuO@Cu$_2$O composites.

consists of slit pores formed by stacking (Fig. S2A). Upon analysis, it can be found that the pore volume of CNT/CuO@Cu$_2$O is significantly reduced compared to CNT. This reduction may be attributed to the selective deposition of copper oxides in specific pores, leading to decreased overall pore volume. Both pore diameters are concentrated around 3.4 nm, and the specific surface area of CNT/CuO@Cu$_2$O is 167.74 m^2 g^{-1} (Fig. S2B). The higher specific surface area and many mesoporous structures provide more adsorption sites for the active molecules, favoring the electrochemical reaction. XRD analysis reveals a diffraction peak at the 2θ = 26.4° position for CNT/CuO@Cu$_2$O and CNT, indicating the presence of the (420) crystallographic plane of C. The diffraction peaks of Cu(CH$_3$COOH)$_2$ are not observed in CNT/CuO@Cu$_2$O. In contrast, the characteristic peaks originally belonging to Cu(CH$_3$COOH)$_2$ are not shown in CNT/CuO@Cu$_2$O. Additionally, several sharp derivative peaks are present in CNT/CuO@Cu$_2$O that are not found in CNT. Matching with the standard diffractograms, it was found that the XRD diffraction peaks of the CNT/CuO@Cu$_2$O composites correspond to copper oxides, respectively. Characteristic peaks of CuO appeared near 2θ of 35.76°, 38.88°, 49°, and 68°, which corresponded to the (−111), (111), (−202), and (−221) crystal planes of CuO, respectively. The diffraction peak at 2θ = 61° corresponded to the (220) crystal plane of Cu$_2$O, further confirming that the spherical nanostructures attached to the surface were attributed to the Cu oxides (Fig. 1E). Raman analysis revealed that the characteristic peaks of copper and CNT existed in the CNT/CuO@Cu$_2$O composites, respectively (Fig. 1F). The D and G peaks of carbon materials were found in CNT/CuO@Cu$_2$O and CNT near 1350 cm^{-1} and 1580 cm^{-1}, respectively. The D to G bands (I_D/I_G) intensity ratio of CNT/CuO@Cu$_2$O was 1.10. At 274 cm^{-1},

the characteristic peak of $Cu(CH_3COOH)_2$ appeared, indicating the presence of copper elements on its surface. FTIR was used to characterize the surface functional groups of CNT/CuO@Cu_2O (Fig. 1G). The absorption peak at 3563.81 cm^{-1} was attributed to the stretching vibration of –OH, while the stretching vibration of C=C was observed at 1641.25 cm^{-1}. The absorption peak at 748 cm^{-1} was attributed to Cu_2O. The results of the FT-IR characterization confirmed the presence of Cu_2O. The presence of Cu_2O was confirmed by the FT-IR characterization results, which initially demonstrated the successful preparation of CNT/CuO@Cu_2O composites.

The prepared composites' composition and the elements' valence states were characterized using X-ray photoelectron spectroscopy (XPS). A more accurate binding energy was obtained using the sp^2 hybridized carbon peak near 284 eV for charge correction. The survey spectrum confirmed the presence of carbon, oxygen, and copper (Fig. 2A). In the high-resolution spectrum of Cu 2p, the peaks at 932.9 eV and 952.5 eV are 3/2 of Cu 2p for CuO and 1/2 of 2p for Cu_2O, which suggests that there is a mixture of oxidation states of +2 and +1, respectively, for this material (Fig. 2B). Meanwhile, the presence of three oscillating satellite peaks with high binding energies at 940.12 eV, 942.59 eV, and 960.98 eV also confirmed the presence of CuO and Cu_2O.[31–33] The fitted peaks of the XPS spectra of C 1s are located at 284 eV, 284.92 eV, 285.86 eV, 287.98 eV, and 282.95 eV for C=C, C–C, C–O, O–C=O, and C–Cu bonds, respectively.[34,35] C–Cu bonds indicate that the copper oxide nanomaterials were successfully incorporated into the CNT structure (Fig. 2C). The XPS spectra of O 1s have three fitted peaks; the peaks at 530.77 eV, 529.06 eV, and 532.31 eV are for Cu_2O, CuO, and oxygen vacancies, respectively, wherein the presence of the oxygen vacancy structure can effectively regulate the CNT/CuO@Cu_2O nanocomposite surface,[35] thus affecting the electron transfer efficiency (Fig. 2D).
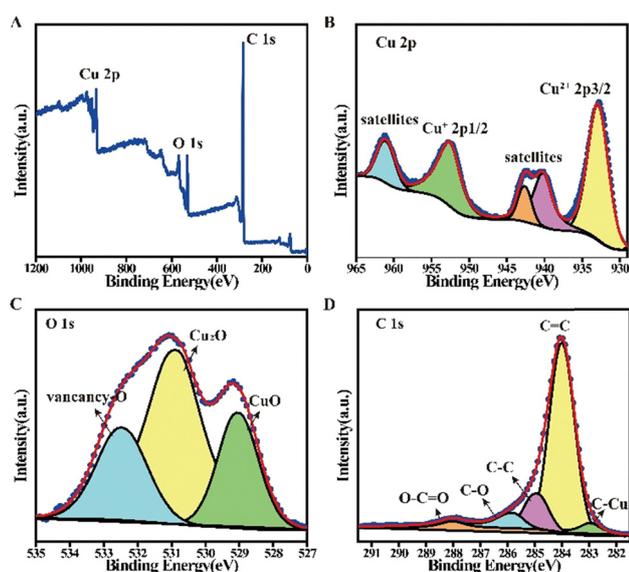

Fig. 2 XPS spectra of (A) the survey spectrum; (B) Cu 2p; (C) C 1s; (D) O 1s of CNT/CuO@Cu_2O composites.

Electrochemical analysis of CNT/CuO@Cu_2O

The electrochemical behaviors of the blank electrode, CNT/GCE, $Cu(CH_3COOH)_2$/GCE, and CNT/CuO@Cu_2O/GCE in PBS buffer, and 0.2 mM creatinine in PBS buffer were analyzed using CV (Fig. 3A). It can be seen that the blank electrode and CNT/GCE have almost no significant current response to creatinine; in contrast, $Cu(CH_3COOH)_2$/GCE has a weak oxidation peak. However, after the introduction of CNT, it can be seen that the current response of $Cu(CH_3COOH)_2$ toward creatinine is much lower than that of CNT/CuO@Cu_2O, and the CNT/CuO@Cu_2O/GCE current density for creatinine was about two times higher than that of the $Cu(CH_3COOH)_2$-modified electrode, indicating that the addition of CNT correspondingly increased the sensitivity of the modified electrode for creatinine detection (Fig. 3B). This proves that the copper group is the active site that reacts with creatinine, and the introduction of intertwined CNT effectively improves the sensing response of copper oxides to creatinine. We fitted the peak oxidation of this material at different sweep speeds and found that the peak current increases linearly with the sweep speed, suggesting a surface-controlled process (Fig. 3C and D). This may be since the introduction of CNT increases the specific surface area of the material, which provides more reaction sites. Because the Cu_2O structure makes it more susceptible to electron transfer, it is more effective in detecting creatinine levels than other materials. As seen in the Nyquist plot of EIS, bare GCE exhibited a semicircle portion with a larger diameter, indicating an increased interfacial charge transfer resistance (Fig. S3A and B). The bare GCE did not show a significant semicircular curve, indicating that the copper-doped CNT material endows the sensor with better electrical conductivity.

To profoundly investigate the detection mechanism of creatinine by CNT/CuO@Cu_2O/GCE, CV analysis of creatinine was carried out by using CNT/CuO@Cu_2O/GCE, and it is apparent from Fig. 3E that the CV curves show two pairs of oxidation peaks, in which the cathodic peak current decreases linearly with increasing creatinine concentration as the creatinine is increased in the range of 0.01 mM to 1 mM. The anodic peak current increased linearly with increasing concentration. Creatinine is reported to be a low electrically active substance, and therefore, direct electron transfer between creatinine and copper oxides is unlikely, so to explain the observed oxidation peaks, it is hypothesized that the mechanism of CNT/CuO@Cu_2O response to creatinine involves a mechanism of copper-creatinine complex formation (Fig. 3F). When the potential is applied, electrochemical oxidation of Cu_2O on the electrode surface occurs, resulting in the formation of Cu^+-creatinine complexes with creatinine through the dispersion of Π-electrons and further oxidation of Cu^{2+}-creatinine complexes and the formation of the complexes leads to a decrease in the concentration of free Cu^+ formed and released from the electrode surface, which leads to an inverse relationship between current and concentration at negative potentials.[36,37] In contrast, at the anodic potential, Cu^{2+} forms complexes with creatinine, which explains why $Cu(CH_3COOH)_2$ has a weak current response to creatinine. The above reasons lead to the

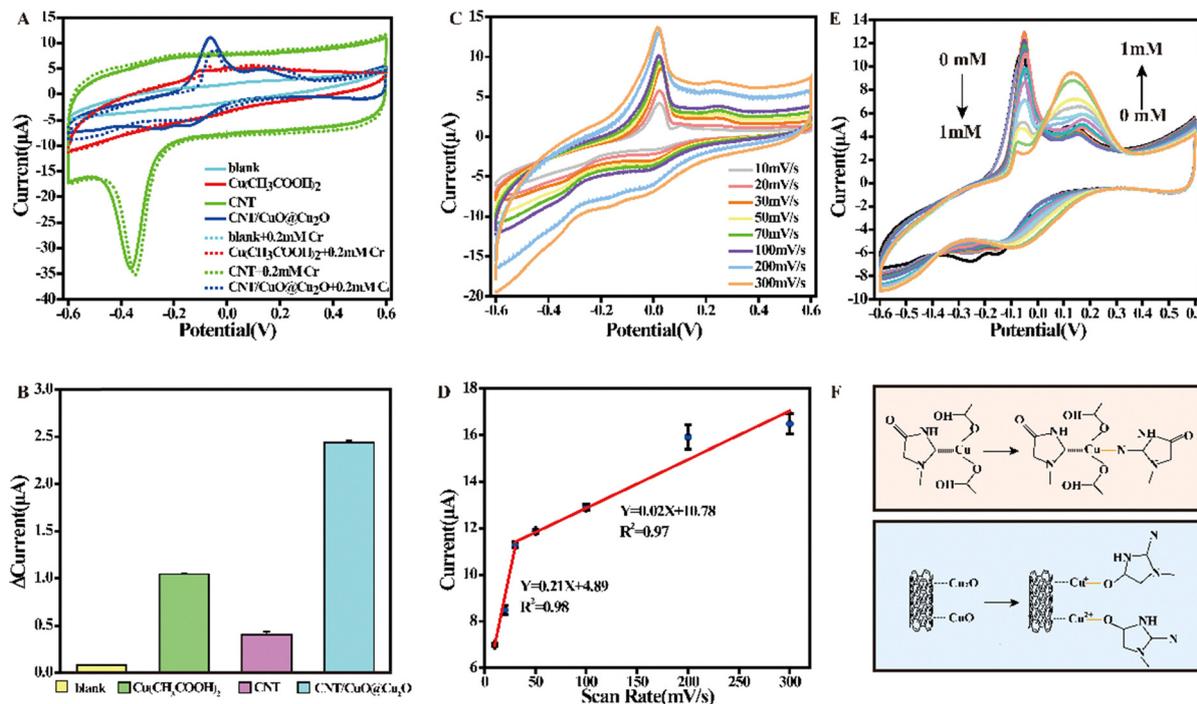**Fig. 3** (A) Comparison of the electrochemical performance of the blank, CNT/GCE, Cu(CH₃COOH)₂/GCE, and CNT/CuO@Cu₂O/GCE in PBS and towards 0.2 mM creatinine in PBS; and (B) histogram of oxidation peak current change; (C) CV recorded at CNT/CuO@Cu₂O/GCE in PBS at a range of scan rates from 10 to 300 mV s^{-1} (inside to outside); (D) linear calibration curve of peak currents *versus* scan rate; (E) CV curves of different concentrations of CNT/CuO@Cu₂O/GCE in PBS; (F) schematic representation of the coordination reaction of copper with creatinine.

formation of a characteristic current with a decreasing peak at negative potentials and an increasing peak at positive potentials.

Detection mechanism

Density functional theory calculations were performed to infer the creatinine detection mechanism. Differential charge density can be used to analyze the charge transfer during adsorption. Yellow indicates the electron aggregation region, and blue indicates the electron deletion region. The adsorption system of CNT, Cu(CH₃COOH)₂, and CNT/CuO@Cu₂O with creatinine (Fig. 4A–C). It can be seen that the adsorption process of copper acetate and CNT/CuO@Cu₂O with creatinine has more electron accumulation compared with CNT, in which mainly the –NH bond of creatinine and C=O realizes the electron transfer to the cuprous ions, indicating that it is mainly the interaction between copper and creatinine in the adsorption process. CNT/CuO@Cu₂O has more electron transfer at the composite interface relative to anhydrous copper acetate, which further indicates that the structure of CNT accelerates the electron transfer rate. Fig. 4D and E show the electronic density of states of copper acetate and CNT/CuO@Cu₂O materials. Relative to Cu(CH₃COOH)₂, the CNT/CuO@Cu₂O composite introduces impurity energy levels in the conduction and valence bands, increasing the probability of electrons reaching the conduction band and its conductivity. Higher localized DOS values were observed in the −1 to −4 eV energy range, which is typical of metals. After CNT modification, the band gap is narrowed, which results in high selectivity and high sensitivity.[38] The adsorption

configurations of creatinine with each material were optimized, and the adsorption energies of creatinine with CNT/CuO@Cu₂O, Cu(CH₃COOH)₂, and CNT were calculated for evaluating their electrochemical performances in creatinine sensors (Fig. 4F–I). The calculated adsorption energies of CNT/CuO@Cu₂O, anhydrous copper acetate and CNT were −0.841, −0.686, and −0.543 eV, respectively, indicating that CNT accelerates the adsorption of anhydride on copper ions, which leads to the electrocatalytic and sensing performance of anhydride, which is a strong indication of the better sensing performance of CNT/CuO@Cu₂O for anhydride.

To attain optimal experimental conditions, the effects of oxygen and pH on CNT/CuO@Cu₂O composites were investigated individually. The CV curves were obtained by saturating PBS with nitrogen and immersing the electrodes in air-saturated and nitrogen-saturated blank PBS electrolytes, as well as PBS electrolytes containing 0.2 mM creatinine (Fig. S4A–D). Comparative analysis revealed that the negative potential current response under nitrogen-saturated conditions was much higher than that under air-saturated conditions for both the blank PBS and the peak oxidation current with the addition of creatinine. This suggests that oxygen in the electrolyte may compete with creatinine. Then, the CV curves illustrate the pH response of CNT/CuO@Cu₂O/GCE at pH 5, 6, 7, 7.4, and 8. Analysis of the peak oxidation currents revealed a decrease with increasing pH. The peak oxidation currents were highest under acidic conditions and notably reduced in an alkaline environment (Fig. S4E). The potential *versus* pH was also compared, and it was found that the maximum potential was −0.06 V at
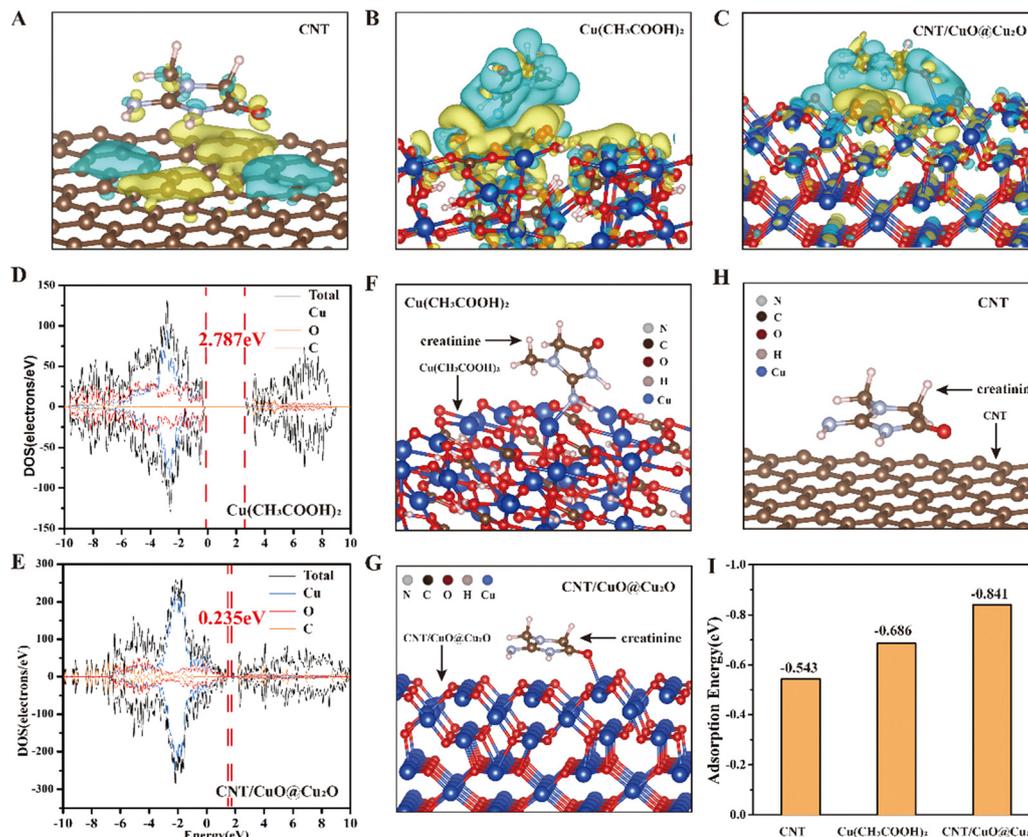
Fig. 4 Differential charge density of (A) CNT, (B) Cu(CH$_3$COOH)$_2$, and (C) CNT/CuO@Cu$_2$O. The density of states (DOS) of (D) Cu(CH$_3$COOH)$_2$ and (E) CNT/CuO@Cu$_2$O, adsorption structure, the adsorption energy histogram of (F) Cu(CH$_3$COOH)$_2$, (G) CNT/CuO@Cu$_2$O, (H) CNT and (I) comparison results.

pH 7.4, which was the lowest potential. After that point, the potential increased positively with the continuous rise in pH (Fig. S4F). Because CNT/CuO@Cu$_2$O/GCE exhibits a distinct redox peak pair in an acidic environment at pH 5, the DPV assay was conducted in PBS buffer at pH 5 and pH 7.4 to achieve the best sensing performance. After conducting the analysis, the results indicated that the sensitivity in an acidic environment was 1672.29 μA mM^{-1} cm^{-2}, significantly lower than that in PBS. Moreover, no clear linear relationship was observed between CNT/CuO@Cu$_2$O and creatinine in the electrolyte with a pH of 5 at a positive potential of 0.17 V (Fig. S5). This indicates the most excellent sensing performance under physiological conditions, which provides a great advantage for detection under physiological samples.

For the different phenomena observed in different air-saturated states and at different pH, the following hypothesis is made (Scheme 1): because of oxygen vacancies in CNT/CuO@Cu$_2$O, the material exhibits significant oxygen adsorption in a humid air setting, leading to further oxidation of Cu$_2$O to CuO under an electric field. At the same time, cuprous oxide reacts with creatinine to form complexes at this potential. Thus, there is a competitive relationship between creatinine and O$_2$. In acidic conditions with a large amount of H$^+$, Cu$_2$O and CuO disproportionates in this environment, forming Cu monomers. This process reduces the concentration of Cu$_2$O, leading to a

lower concentration of Cu+ available to react with creatinine. Consequently, there is a decrease in electrocatalytic activity, resulting in lower sensitivity at pH 5 and a minimum potential at pH 7.4. At pH 7.4, the detector can more easily acquire electrons to be oxidized by creatinine at a low electric potential. Under these conditions, detectors are more likely to oxidize electrons. CNT/CuO@Cu$_2$O exhibits the highest electron transfer activity under physiological conditions and demonstrates the most significant sensitivity.

**Performance study of CNT/CuO@Cu$_2$O sensors**

Fig. 5A displays the amperometric response of the CNT/CuO@Cu$_2$O nanocomposite to creatinine under optimal experimental conditions. We added 0.01–1 mM creatinine concentrations dropwise into PBS using DPV to measure the corresponding oxidation peak currents. After analyzing the fit, we classified the biosensor's response to the creatinine concentration into three linear regions, each with a different slope (Fig. 5B). The relationship can be expressed by the following linear regression equation:

$$Y = -603.25X + 83.40 \quad (R^2 = 0.99) \tag{1}$$

$$Y = -92.68X + 53.18 \quad (R^2 = 0.95) \tag{2}$$

$$Y = -21.39X + 22.71 \quad (R^2 = 0.99) \tag{3}$$
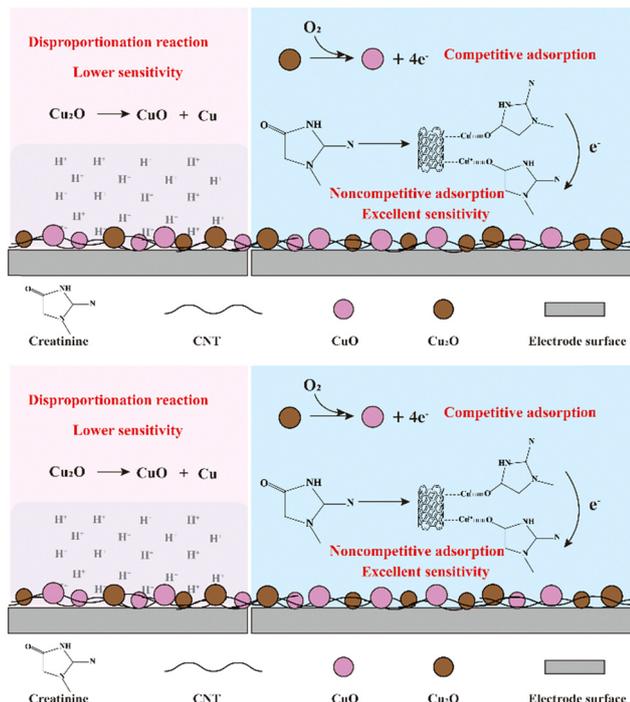
Scheme 1 Detection mechanism diagram of a CNT/CuO@Cu$_2$O composite electrochemical sensor with creatinine.

Fig. 5 (A) Typical DPV voltammograms obtained using CNT/CuO@Cu$_2$O/GCE electrode for sensing the different concentrations of creatinine from 0.01 mM to 1 Mm; (B) calibration plot of the cathode peak current *vs.* creatinine concentration; selectivity detected by (C) DPV response and (D) histogram profile of CNT/CuO@Cu$_2$O/GCE with diverse interferences containing creatine, urea, glucose, NaCl and KCl.

Y is the measured peak DPV current at a negative potential, and *X* is the creatinine concentration. The regression coefficients (R^2) are obtained from three replicate measures (n = 3). The values for (1), (2), and (3) are 0.99, 0.95, and 0.99 respectively, indicating high regression accuracy. The detection limit of the CNT/CuO@Cu$_2$O sensor for creatinine was calculated to be 0.002 mM, and the most heightened sensitivity was 8617.86 μA mM^{-1} cm^{-2} at a creatinine concentration of 0.01 to 0.05 mM. Due to their large specific surface area, carbon nanotubes offer numerous adsorption sites for copper and cuprous ions. This allows related copper ions to adsorb more creatinine and form complexes, which may contribute to the ultra-sensitive response to creatinine exhibited by electrodes prepared using this material. The sensor also showed a high linear response at a positive potential with a detection limit of 0.2 mM and a maximum sensitivity of 643.57 μA mM^{-1} cm^{-2} (Fig. S6). Additionally, the CNT/CuO@Cu$_2$O sensor demonstrated excellent selectivity for creatinine in various interferences (Fig. 5C and D). To test the sensor's performance under different conditions, we added 0.2 mM concentrations of creatinine and interfering substances to 10 mL of PBS, ensuring urea, glucose, NaCl, and KCl were present along with creatinine. The interfering substances were all at the highest concentrations in serum. The sensor exhibited better interference ability and accuracy. Furthermore, we conducted reproducibility experiments using the DPV response (Fig. S7) for five modified electrodes, demonstrating good reproducibility. This further substantiates the superiority of CNT/CuO@Cu$_2$O as a sensing material.

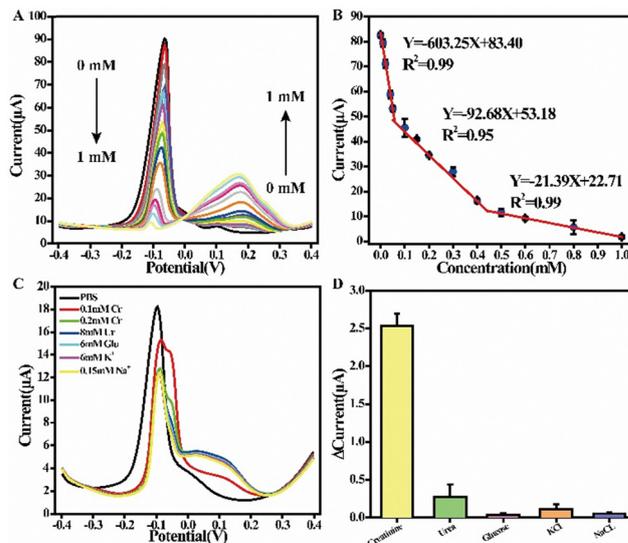The reported nanomaterial-based creatinine sensors and their sensitivity, limit of detection (LOD), and response range, are listed in Table 1, indicating that the CNT/CuO@Cu$_2$O/GCE sensor shows the highest sensitivity and very low LOD. In addition, to demonstrate the reproducibility and stability of the electrode, the prepared sensors were evaluated through measuring the DPV current responses using 10 mL solution containing PBS 0.1 M and creatinine 0.2 mM in various sensors (No. 1, 2, 3, 4, 5) and various times (0, 1, 2, 7, 10, 15, 20, 30, 40 and 60 days). After different times of storage at 4 °C, the DPV measurements were done three times and their average was utilized as the data for evaluation of the sensor's reproducibility (Fig. S7) and stability (Fig. S8). As seen in Fig. S7, no significant discrepancy was observed in current responses. For stability, only changes were obtained for DPV measurements using the CNT/CuO@Cu$_2$O/GCE sensor after 60 days, so that the value of current decreased from 15.88 μA to 15.31 μA (96.41% obtained, 3.59% decrease) and voltage deviation from −0.1123 V to −0.1595 (142.03% deviation) after sixty days (Table S1). During the storage time, the average value of sensor current change is 15.63 ± 0.18 μA, and mean percentage of the original current retained is 98.42% ± 1.12%. About potential change, the average value is −0.1343 ± 0.019 V, and the mean percentage of voltage deviation is 119.61% ± 16.65%. This indicated the perfect stability of the prepared sensor surfaces. So, the prepared sensors can be attributed to the high stability of creatinine sensors.

Application

Various types of flexible sensors were fabricated using this material in two different ways. The first electrode was fabricated using a 3D printing technique. It consisted of a composite ink made from CNT/CuO@Cu$_2$O with carbon paste, serving as the working electrode and counter electrode. Fig. S9A illustrates

Table 1 Comparison of our work with different electrochemical sensors for creatinine detection

Electrode	LOD [mM]	Response range [mM]	Sensitivity [$\mu A\ mM^{-1}\ cm^{-2}$]	Ref.
B/carbon-graphite	0.83	0.05–1.40	11.82	14
Carbon black film/Fe^{3+}	0.043	0.10–6.50	41.57	39
CuO-IL/rGO	0.037	0.50–35	0.53	20
NPG/GCE	0.01	0.01–2	195.05	40
Fe–Cu–rGO@Ag	1×10^{-5}	1×10^{-5}–1.0	1100	41
ZIF-8 NPs	0.03	0.05–2.5	101.11	17
Multi-enzyme/c-MWCNT/PANI/Pt	0.0001	0.01–0.75	12.0	42
PTA/PEI multilayer	6×10^{-5}	0–0.0625	—	43
Au/SPCE	7.2×10^{-7}	0–0.0088	470.0	44
PTSPCE/CuNPs	0.0001	0.01–0.169	258.20	45
Ferrocyanide/SPCEs	0.06	4.0–15.0	21.0	46
PAA gel-Cu(II)/Cu_2O NPs	0.0065	0.20–100	—	47
CNT/CuO@Cu_2O/GCE	0.002	0.01–1	8617.86	This work
Flexible sensors	0.01	0.01–1	584.8	This work

the preparation process and images of the flexible sensors. Additionally, 3D flexible sensors printed using pure carbon paste were also prepared. By dropping 100 μL of PBS on the working electrode for cyclic voltammetry (CV) scanning, the CNT/CuO@Cu_2O composite ink exhibits a larger surface area compared to the pure carbon paste electrode. This suggests that the composite ink, prepared from this material, offers improved sensing performance over the carbon paste (Fig. S9B). Different concentration gradients of creatinine were added to the solution, and it was observed that the flexible electrode demonstrated an excellent linear response to creatinine (Fig. S9C and D) over a wide linear range (0.1–30 mM). The second approach involves constructing a flexible sensor by sputtering a gold layer on PET as a conductive circuit. This method offers the advantage of greater stability compared to the first approach, where the conductive layer is prone to detachment. By dropping 200 μL of PBS on the working electrode for CV scanning, the CNT/CuO@Cu_2O electrode exhibits a larger cyclic area compared to the blank gold electrode, suggesting a higher capacitance (Fig. 6A). Meanwhile, by comparing the changes in oxidation peak current of the blank gold electrode and the CNT/CuO@Cu_2O gold electrode after adding 0.2 mM creatinine, it was observed that the response of the blank gold electrode to creatinine was very weak, significantly smaller than the current response of the CNT/CuO@Cu_2O gold electrode to creatinine (Fig. 6B). The DPV analysis was conducted by introducing various creatinine concentrations. The oxidation peak current decreased linearly as the creatinine concentration increased (Fig. 6C). This trend aligned with the observations on the glassy carbon electrode, suggesting that the catalytic site remained Cu_2O. The fitting analysis revealed that the sensitivity could reach up to 584.8 μA mM^{-1} cm^{-2} in the physiological concentration range, which was close to the sensitivity of the commercial silk-screen electrodes. This suggests that printed electrodes' sensitivity is comparable to commercial screen electrodes, indicating excellent sensing performance. To investigate the creatinine detection ability of the CNT/CuO@Cu_2O gold electrode at different bending angles, the CV response in PBS containing 0.1 mM creatinine was recorded in the relaxed state (0°) and at three bending angles (15°, 30°, and 60°) (Fig. 6D). After bending 60°, 82.5% of the relaxed state can still
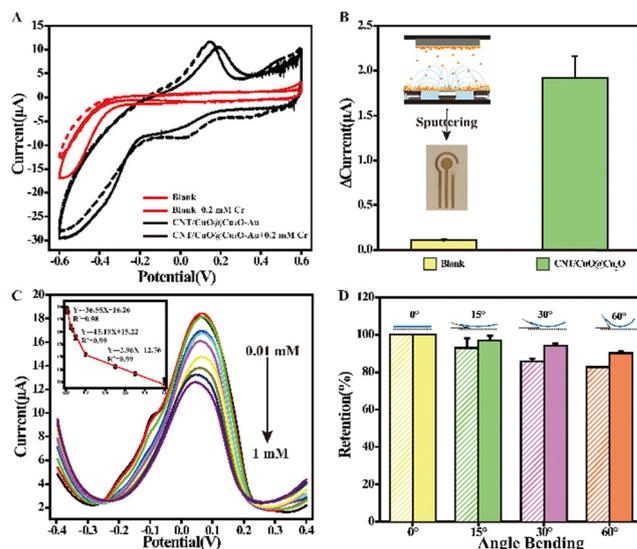

Fig. 6 CV response of the blank gold electrode and CNT/CuO@Cu_2O gold electrode (A) in PBS and with the addition of 0.2 mM creatinine, respectively; (B) histogram of the current change after the addition of 0.2 mM creatinine, the picture attached is a photograph of the gold electrode; (C) linear calibration curve of the CNT/CuO@Cu_2O gold electrode after adding different concentrations of creatinine, illustrated as the DPV curve diagram; (D) bar chart of comparison of CNT/CuO@Cu_2O gold electrodes in PBS containing 0.1 mM creatinine at bending angles of 0°, 15°, 30° and 60°.

be reached, and the RSD value is 2.57%, and the RSD of the relaxed state is 1.7% after bending, indicating that the flexible sensor has good mechanical properties.

Testing of serum samples

The 3D printed flexible electrode CNT/CuO@Cu_2O based biosensor, was utilized for the quantification of creatinine levels in serum samples, thereby evaluating its suitability for practical diagnostic applications. Serum samples from rats were procured, and subsequent spiked recovery experiments were performed to ascertain the efficacy of CNT/CuO@Cu_2O in the analysis of creatinine. As delineated in Table S2, a comparative analysis was conducted between the creatinine concentrations determined *via* the CNT/CuO@Cu_2O assay and the known quantities of creatinine introduced into the samples. The

analytical data revealed that the recoveries of spiked creatinine samples spanned between 88% and 110%. These findings underscore the sensor's detection prowess and corroborate the potential utility of the non-enzymatic sensor fabricated from CNT/CuO@Cu$_2$O in clinical settings.

Conclusions

We prepared an enzyme-free electrochemical creatinine sensor using a one-step hydrothermal method, which involved functionalizing a carbon nanotube with anhydrous copper acetate. The sensor exhibits excellent electrochemical properties, with a detection limit of 0.002 mM and a sensitivity of 8617.86 μA mM^{-1} cm^{-2}. The dense network structure formed by the intertwining of CNT significantly increased the specific surface area and provided many adsorption sites for the coordination reaction of copper nanoparticles with creatinine. This, in turn, leads to an exceptionally high sensitivity of the CNT/CuO@Cu$_2$O sensor. Additionally, it exhibited excellent sensing performance on the screen-printed electrode and good recovery rates when the assay was spiked in serum. The flexible creatinine sensors prepared using various methods also exhibit good sensing performance. The composite electrode has higher sensitivity and sensing performance, suggesting that CNT/CuO@Cu$_2$O has excellent potential in healthcare.

Author contributions

Taotao Liang and Lin Guo initiated the concept and designed the overall studies. Lin Guo and Xiaogang Guo supervised the work. Taotao Liang, Yan Zhang and Chuyue Tang led the experiments and collected the overall data. Junfeng Guo contributed to sensor characterization and validation. Tao Hu provided the usage permission for the theoretical calculation software armor. All authors contributed to the data analysis and provided feedback on the manuscript.

Conflicts of interest

There are no conflicts to declare.

Data availability

The raw data supporting the conclusions of this article will be made available by the authors on request.

Supplementary information is available. See DOI: https://doi.org/10.1039/d5ma00644a.

Acknowledgements

Notes and references

1 A. Levin, S. Ahmed, J. Carrero, B. Foster, A. Francis, R. Hall, W. Herrington, G. Hill, L. Inker, R. Kazancıoğlu, E. Lamb, P. Lin, M. Madero, N. McIntyre, K. Morrow, G. Roberts, D. Sabanayagam, E. Schäeffner, M. Shlipak, R. Shroff, N. Tangri, T. Thanachayanont, I. Ulasi, G. Wong, C. Yang, L. Zhang, K. Robinson, L. Wilson, R. Wilson, B. Kasiske, M. Cheung, A. Earley and P. Stevens, *Kidney Int.*, 2024, **105**, 684–701.

2 L. Appel, M. Grams, M. Woodward, K. Harris, H. Arima, J. Chalmers, H. Yatsuya, K. Tamakoshi, Y. Li, J. Coresh, Y. Sang, K. Matsushita, K. Polkinghorne, S. Chadban, A. Levin, O. Djurdjev, M. Tang, L. Zhang, F. Wang, J. Wang, M. Zhao, E. Schäeffner, N. Ebert, N. Mielke, M. Tonelli, A. Lloyd, F. Sacks, M. Shlipak, N. Bansal, M. Sarnak, K. Yamagishi, I. Muraki, Y. Shimizu, H. Iso, M. Fukagawa, S. Maruyama, T. Hamano, N. Fujii, T. Imaizumi, N. Pinho, M. Metzger, B. Stengel, A. Hamroun, Z. Massy, T. Jafar, I. Jehan, J. Hatcher, N. Chaturvedi, N. Poulter, D. Wheeler, M. Landray, A. Anderson, J. Chen, J. Lash, J. Taliercio, P. Yang, K. Tuttle, R. Alicic, S. Nicholas, J. Shen, B. Schöttker, H. Stocker, D. Rothenbacher, H. Brenner, D. Levy, S. Hwang, M. Schneider, A. Köttgen, H. Meiselbach, K. Eckardt, A. Chang, J. Green, H. Kirchner, G. Singh, S. Sawhney, C. Black, K. Wilde, A. Marks, S. Bell, M. Siddiqui, C. Palmer, E. Pearson, M. Miyazaki, M. Nakayama, T. Yamamoto, G. Yamada, S. Ito, M. Círillo, A. Wang, H. Wu, H. Cheung, V. Ngai, T. Tak, A. Garg, E. McArthur, A. Young, V. Jha, A. Yadav, V. Kumar and A. Carson, *JAMA*, 2023, **330**, 1266.

3 R. Canovas, M. Cuartero and G. A. Crespo, *Biosens. Bioelectron.*, 2019, **130**, 110–124.

4 S. Singh, S. Bhardwaj, P. Tiwari, K. Dev, K. Ghosh and P. K. Maji, *Mater. Adv.*, 2024, **5**, 2622.

5 M. Sarwal and M. Naesens, *Kidney Int.*, 2023, **104**, 432–439.

6 K. F. Kayani, S. J. Mohammed, D. Ghafoor, M. K. Rahim and H. R. Ahmed, *Mater. Adv.*, 2024, **5**, 4618.

7 P. Jayasekhar Babu, A. Tirkey, T. J. Mohan Rao, N. B. Chanu, K. Lalchhandama and Y. D. Singh, *Anal. Biochem.*, 2022, **645**, 114622.

8 S. S. Timilsina, M. Ramasamy, N. Durr, R. Ahmad, P. Jolly and D. E. Ingber, *Adv. Healthcare Mater.*, 2022, **11**, e2200589.

9 K. Sideeq Bhat, H. Kim, A. Alam, M. Ko, J. An and S. Lim, *Adv. Healthcare Mater.*, 2021, **10**, e2101193.

10 T. Liang, L. Zou, X. Guo, X. Ma, C. Zhang, Z. Zou, Y. Zhang, F. Hu, Z. Lu, K. Tang and C. M. Li, *Adv. Funct. Mater.*, 2019, **29**, 1903026.

11 S. Li, J. Dai, M. Zhu, N. Arroyo-Currás, H. Li, Y. Wang, Q. Wang, X. Lou, T. Kippin, S. Wang, K. Plaxco, H. Li and F. Xia, *ACS Nano*, 2023, **17**, 18525–18538.

12 F. Mota, M. Passos, J. Santos and M. Saraiva, *Biosens. Bioelectron.*, 2024, **251**, 116095.

13 K. Wang, Q. Ding, M. Qi, W. Zhang, Y. Hou, R. Cao, C. Li, L. Xu, L. Wang and J. Kim, *Adv. Funct. Mater.*, 2024, **34**, 2316820.

14 Y. Dong, X. Luo, Y. Liu, C. Yan, H. Li, J. Lv, L. Yang and Y. Cui, *Talanta*, 2022, **248**, 123592.

15 J. Mao, Z. D. He, Y. Z. Wu, J. W. Cao, S. J. Zhao, B. Chen, Y. W. Liu and R. W. Li, *Adv. Funct. Mater.*, 2018, **5**, 5813.

16 P. Dasgupta, V. Kumar, P. R. Krishnaswamy and N. Bhat, *ACS Omega*, 2020, **5**, 22459–22464.

17 T. Chakraborty, M. Das, C. Y. Lin, Y. Su, B. Yuan and C. H. Kao, *Membranes*, 2022, **12**, 159.

18 J. Yang, H. L. Ye, F. Q. Zhao and B. Z. Zeng, *ACS Appl. Mater. Interfaces*, 2016, **8**, 20407.

19 K. A. Deo, M. K. Jaiswal, S. Abasi, G. Lokhande, S. Bhunia, T. U. Nguyen, M. Namkoong, K. Darvesh, A. Guiseppi-Elie, L. Tian and A. K. Gaharwar, *ACS Nano*, 2022, **16**, 8798–8811.

20 K. Teekayupak, C. Aumnate, A. Lomae, P. Preechakasedkit, C. S. Henry, O. Chailapakul and N. Ruecha, *Talanta*, 2023, **254**, 124131.

21 M. Abidian, *Adv. Sci.*, 2024, **11**, 2404458.

22 L. Florea, E. Blasco and V. Mattoli, *Adv. Funct. Mater.*, 2023, **33**, 2305697.

23 Z. Wang, L. Zeng, X. Mei, L. Cai, K. Lin, J. Rodríguez, Z. Ye, X. Parraguez, E. Guajardo, P. Luna, J. Zhang and Y. Zhang, *Adv. Mater.*, 2025, **37**, 2416260; G. Wei, L. Wang, L. Huo and Y. Zhang, *Talanta*, 2020, **209**, 120431.

24 P. Ananthasubramanian, P. J. Bora, C. Gadadasu, P. C. Ramamurthy and N. Raghavan, *Mater. Adv.*, 2025, **6**, 4299.

25 S. Freddi, A. V. Emelianov, I. I. Bobrinetskiy, G. Drera, S. Pagliara, D. S. Kopylova, M. Chiesa, G. Santini, N. Mores, U. Moscato, A. G. Nasibulin, P. Montuschi and L. Sangaletti, *Adv. Healthcare Mater.*, 2020, **9**, e2000377.

26 G. Dandegaonkar, A. Ahmed, L. Y. Sun, B. Adak and S. Mukhopadhyay, *Mater. Adv.*, 2022, **3**, 3766.

27 Y. Li, L. Luo, Y. Kong, S. George, Y. Li, X. Guo, X. Li, E. Yeatman, A. Davenport, Y. Li and B. Li, *Adv. Funct. Mater.*, 2024, **34**, 2316865.

28 H. Dehghan-Manshadi, M. Mazloum-Ardakani and S. Mozaffari, *Biosens. Bioelectron.*, 2023, **246**, 115881.

29 R. Manikandan, M. Kim, H. Jang, A. Mugunthan, C. Kim, J. Yoon, J. Lee, K. Chung and S. Chang, *Biosens. Bioelectron.*, 2024, **271**, 117075.

30 L. Parra, G. Laucirica, M. Toimil-Molares, W. Marmisollé and O. Azzaroni, *Biosens. Bioelectron.*, 2024, **268**, 116893.

31 J. Lv, C. Kong, Y. Xu, Z. Yang, X. Zhang, S. Yang, G. Meng, J. Bi, J. Li and S. Yang, *Sens. Actuators, B*, 2017, **248**, 630–638.

32 P. Yang, X. Wang, C.-Y. Ge, X. Fu, X. Y. Liu, H. Chai, X. Guo, H.-C. Yao, Y. X. Zhang and K. Chen, *Appl. Surf. Sci.*, 2019, **494**, 484–491.

33 C. Yu, J. Cui, Y. Wang, H. Zheng, J. Zhang, X. Shu, J. Liu, Y. Zhang and Y. Wu, *Appl. Surf. Sci.*, 2018, **439**, 11–17.

34 Y. Peng, M. Li, X. Jia, J. Su, X. Zhao, S. Zhang, H. Zhang, X. Zhou, J. Chen, Y. Huang, T. Wagberg and G. Hu, *ACS Appl. Mater. Interfaces*, 2022, **14**, 28956–28964.

35 L. Ding, F. Yan, Y. Zhang, L. Liu, X. Yu and H. Liu, *ACS Appl. Nano Mater.*, 2019, **3**, 617–623.

36 S. Kalasin, P. Sangnuang, P. Khownarumit, I. M. Tang and W. Surareungchai, *ACS Biomater. Sci. Eng.*, 2020, **6**, 1247–1258.

37 R. K. Rakesh Kumar, M. O. Shaikh, A. Kumar, C.-H. Liu and C.-H. Chuang, *ACS Appl. Nano Mater.*, 2023, **6**, 2083–2094.

38 J. Wang, Y. Ren, H. Liu, Z. Li, X. Liu, Y. Deng and X. Fang, *Adv. Mater.*, 2022, **34**, e2104958.

39 E. L. Fava, T. M. D. Prado, A. Garcia-Filho, T. A. Silva, F. H. Cincotto, F. Cruz de Moraes, R. C. Faria and O. Fatibello-Filho, *Talanta*, 2020, **207**, 120277.

40 M. A. Cardona-Castro, J. A. Leon-Gil and J. Alvarez-Quintana, *Mater. Adv.*, 2021, **2**, 5942.

41 P. Singh, S. Mandal, D. Roy and N. Chanda, *ACS Biomater. Sci. Eng.*, 2021, **7**, 3446–3458.

42 S. Yadav, A. Kumar and C. S. Pundir, *Anal. Biochem.*, 2011, **419**, 277–283.

43 P. Han, S. Xu, S. Feng, Y. Hao and J. Wang, *Talanta*, 2016, **151**, 114–118.

44 A. Diouf, S. Motia, N. Alami Hassani, N. Bari and B. Bouchikhi, *J. Electroanal. Chem.*, 2017, **788**, 44–53.

45 A. Domínguez-Aragón, A. S. Conejo-Dávila, E. A. Zaragoza-Contreras and R. B. Dominguez, *Chemosensors*, 2023, 11.

46 S. Bajpai, G. Akien and K. Toghill, *Electrochem. Commun.*, 2023, **158**, 107624.

47 S. Kalasin, P. Sangnuang, P. Khownarumit, I. Tang and W. Surareungchai, *ACS Biomater. Sci. Eng.*, 2020, **6**, 1247–1258.